Laser Patterning Captured in Real-Time: Surface Modifications of Multilayer Thin-Films Under Nanosecond Laser Heating

Journal:	*Nanoscale*
Manuscript ID	NR-ART-03-2024-001378.R1
Article Type:	Paper
Date Submitted by the Author:	30-Jul-2024
Complete List of Authors:	Isik, Tugba; Purdue University, Mechanical Engineering Freund, Mason; University of Connecticut, Materials Science and Engineering Linthicum, Will; University of Connecticut, Materials Science and Engineering Huey, Bryan; University of Connecticut, Materials Science and Engineering Ortalan, Volkan; University of Connecticut, Materials Science and Engineering

ARTICLE

Laser Patterning Captured in Real-Time: Surface Modifications of Multilayer Thin-Films Under Nanosecond Laser Heating

Tugba Isik,[†a] Mason Freund,[b] Will Linthicum,[b] Bryan D. Huey[b] and Volkan Ortalan *[b]

Received 00th January 20xx,
Accepted 00th January 20xx

DOI: 10.1039/x0xx00000x

Controlled wrinkle formation has attracted intensive research interest as a means to modify surface properties. However, most of the currently explored methods rely on mechanically stretching polymer substrates with hard surface coatings, and the application of these methods to different materials is limited. Here, for the first time, we demonstrate laser-assisted periodic wrinkle formation on silicon nitride (SiN) membranes that are coated with titanium (Ti)/nickel (Ni) multilayers. Corrugated surface formation mechanism, as well as grain nucleation and growth, are studied using ultrafast transmission electron microscopy (UTEM). Periodic wrinkling and patterning of multilayers on thin SiN membranes are induced by a nanosecond pulsed laser, and the deformation of the film is captured by single-shot imaging. The investigated structures revealed periodic wrinkling of the membrane and corrugated surface formation on both sides of the film. The findings of this work could allow laser-irradiation-based fast fabrication of corrugated films with tailored properties.

Introduction

Apart from being considered as a manufacturing defect that needs to be fixed, surface wrinkling is often utilized as a tool for thin-film characterization and functional micro-structuring. Mechanical instabilities in thin-films have been studied for years, both to discover the underlying mechanics, and to enable the fabrication of these topological features in a well-defined configuration. Carefully engineered surface wrinkles can modify the optical properties of the surface, enhance adhesion,[1] and control wettability,[2–4] making these structures appealing for various applications such as photonics, microfluidics, stretchable electronics, biosensors, and others.[5–7] It was also shown that the characteristic length scale of highly ordered surface wrinkles depends on and can be used to measure material properties such as Poisson's ratio, elastic modulus, and residual stress.[5,8,9]

Wrinkle formation in thin-films takes place under compressive stress and can be triggered via capillary forces, solvent diffusion, mechanical stretching, or thermal mismatch.[6,10–13] Their formation mechanism has been extensively studied, and various numerical theories were developed to obtain an expression for wrinkle wavelength and amplitude.[8,14–16] Experimental researchers have focused on tailoring wrinkle morphologies for specific applications via mechanically deforming the wrinkled substrate, guiding the buckle orientation by using a non-planar mold, or adding topographical structures to the substrate before deposition of the second layer.[17] Despite being established as a quick and versatile method for the fabrication of micrometer and nanometer sized surface structures in a controlled manner,[18–23] the application of pulsed lasers for periodic wrinkle formation has been very limited.

Well-tailored laser-induced fabrication of surface structures requires a comprehensive analysis that considers laser-matter interactions as well as liquid motion in cases of melting. Ultrafast transmission electron microscopy (UTEM) offers the potential for significant insights into the fundamental processes in rapid irreversible reactions in various material systems. While samples are excited with a pulsed laser to trigger reactions (with pulse widths from femtoseconds to nanoseconds), a second laser pulse with a known time delay is used to stimulate the photoemission of an electron pulse from the cathode (Fig. 1(a)). The resulting intense pulse of electrons enables snapshot images or diffraction patterns to be collected with high temporal resolution at well-defined delay times. By repeating this single-shot approach in fresh sample regions at different time delays, it is possible to capture the various stages of high-speed irreversible processes, which has been successfully applied to a series of non-equilibrium events that happened at the nanoscale.[24–39]

In this work, the effect of nanosecond pulsed laser heating on multilayer thin films is studied with UTEM. We demonstrate laser-induced periodic wrinkling on thin silicon nitride (SiN) membranes coated with Ti/Ni multilayers and discuss the effect of substrate and metal layer properties on the final morphology. The evolution of the surface structures is captured at different time delays with single-shot images in a pump-probe scheme. The final wrinkled multilayer structures are investigated using atomic force microscopy (AFM) topography mapping,

---

[a] School of Mechanical Engineering, Purdue University, West Lafayette, Indiana 47907, USA.
[b] Department of Materials Science & Engineering, University of Connecticut, Storrs, Connecticut 06269, USA. E-mail: vortalan@uconn.edu
† Current address: X-ray Science Division, Advanced Photon Source, Argonne National Laboratory, Argonne, IL 60439, USA.

Electronic Supplementary Information (ESI) available: See DOI: 10.1039/x0xx00000x

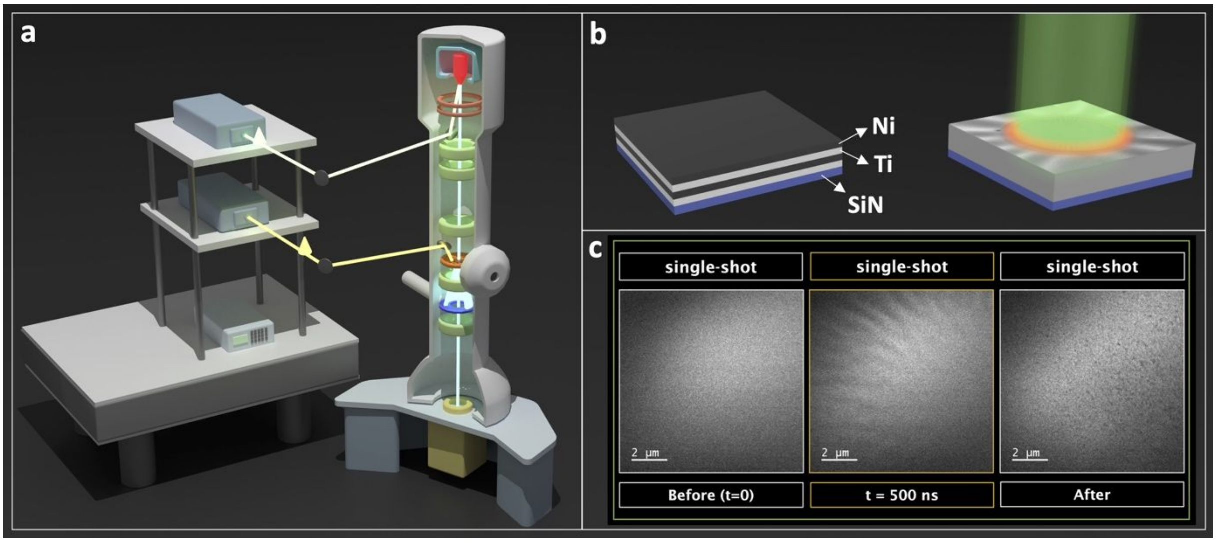

Fig. 1 (a) Schematic of UTEM used for the single-shot experiments. (b) The initial structure of the multilayer film and illustration of the laser heating. (c) Single-shot data collected at 500 ns time delay from an area close to the center of the laser beam showing a transient structure (middle), alongside before and after single-shot images.

transmission electron microscopy (TEM), scanning electron microscopy (SEM), and energy dispersive x-ray spectroscopy (EDX). Thermal and mechanical buckling simulations based on finite element method (FEM) provide complementary evidence in support of the proposed dynamic mechanisms.

Experimental Section

Materials

Thin-film samples were prepared by coating alternating layers of Ti and Ni on SiN TEM grids with electron beam evaporation (Fig. 1(b)). To explore the influence of the support membrane thickness, we worked with both 15 nm and 50 nm thick SiN membranes. Individual layer thicknesses were designed to achieve a 2:3 atomic ratio (Ti:Ni), and each membrane was coated with two bilayers, four layers in total, under the same conditions (See Supporting Information). The total thickness of the metal films was kept to around 50 nm.

Results and Discussion

We performed the time-resolved imaging at a magnification that allows a field of view of approximately 100 μm^2. This is ideal for viewing the dynamic process in and around the irradiated region, even though it precludes resolving the initial grain sizes (9.5 nm on average) for the as-deposited multilayer films before any localized laser heating. Fig. 1(c) shows a collage of images collected from an area close to the laser spot center, for a sample prepared on a 15 nm SiN substrate. The dynamic reaction was captured 500 ns after the sample excitation laser pulse (wavelength of 532 nm, pulse width of 1 ns, and spot size of ~80 μm) interacted with the specimen. While the comparison of before and after images indicates an increased grain size at the center of the laser spot, the single-shot image collected with 500 ns delay reveals a transient structure which suggests a more complex dynamic process. These transient 'cellular structures' seem to be initiated from the laser center, elongating towards the periphery shortly after the laser pulse, and disappearing towards the end of the dynamic reaction process. This indicates the presence of a secondary process unrelated to grain nucleation and growth. To understand this dynamic process, we next positioned the laser spot approximately 20-25 μm away from the observation point and collected a series of single-shot images similar to those in Fig. 1. Fig. 2 illustrates a dataset collected with a 4500 ns delay time where there is a shift between the sample excitation laser spot and the optical axis of the electron pulse. To emphasize this lateral spatial shift, the direction of the laser center is shown by the dashed yellow arrow, while the solid red arrow points toward the edge of the illuminated region. All other panels in Fig. 2 present the same location, but with the superimposed guides omitted for clarity (See Fig. S1 for more details).

As seen in Fig. 2, the cellular structures previously observed at the laser center become more pronounced at the edge exhibiting higher contrast and order. The comparison of the after image with the one collected at a 4500 ns time delay gives more details about the final structure, which was not detected when the TEM field of view was coincident with the laser

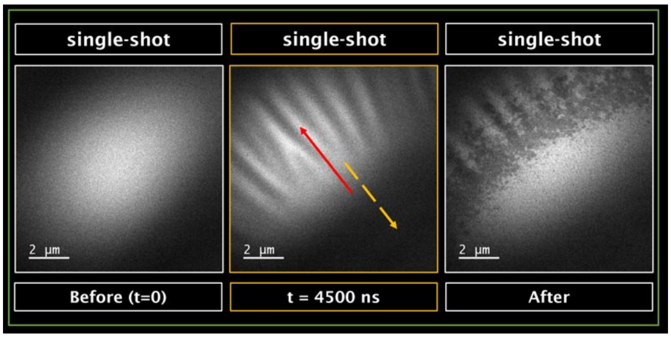

Fig. 2 Single-shot data collected from the edge of the laser spot at 4500 ns (4.5 μs). The dashed yellow arrow is pointing towards the laser beam center, and the solid red arrow indicates the propagation direction of the cellular structures.

illumination point. At this time delay, the cellular structures are visible close to the edge with a longer length than observed in the after image. This shows that the transient cellular structures have started forming at the center, propagated toward the edge of the irradiated region, while nearer the center the film has recovered to near its original state except with increased average grain size (around seven times). At the end, the same cellular features are still partially present, though only nearest the periphery, with the other features replaced by an apparent ring of markedly increased grain sizes.

These morphological changes do not happen concurrently; in fact, capturing the grain nucleation and growth process requires longer delay times. With this objective in mind, we investigated the structural changes between 4.5 µs - 15 µs on multiple samples, with the key results displayed in Fig. 3(a-c). The cellular features consist of small grains at 6.5 µs. At around 8.5 µs, larger grains appear at the outer edge, and with time, they start to grow towards the center (visible at around 15 µs). Finally, the growth of these lateral crystals is followed by the formation of equiaxed grains all around the cellular structures. Lateral crystal growth in thin TiNi films under pulsed laser heating is known to be a melt-mediated crystallization technique.[40] After complete melting, the temperature at the melt boundary drops slightly below the melting temperature, and unmelted seeds start growing into the neighboring molten regions. This theory explains the crystal growth direction observed in UTEM experiments and proves that the heated region completely melts under the laser pulse, including the part where the cellular structures are frozen in place.

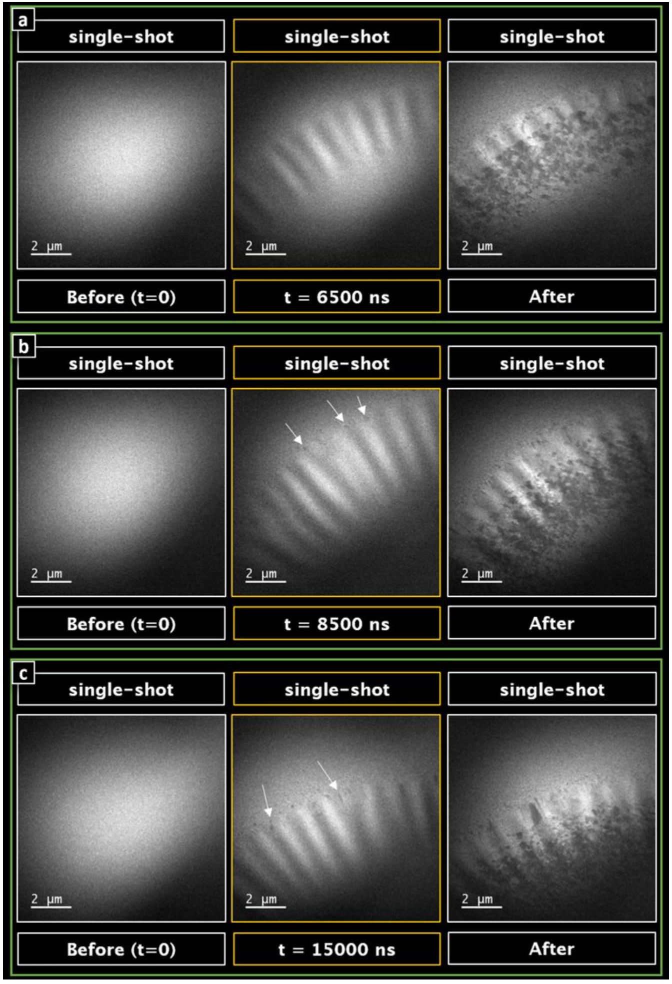

Fig. 3 A collage of single-shot images collected between 4.5 µs and 15 µs showing grain formation at the edge of the laser-irradiated region. The delay times are (a) 6500 ns, (b) 8500 ns, and (c) 15000 ns.

Post-mortem TEM imaging of the samples (Fig. 4(a)) reveals that the detected transient structures are frozen all around the periphery of the laser-heated zone. The variation in grain structure and periodic contrast undulation along the azimuthal angle are more apparent in high-angle annular dark-field (HAADF) scanning transmission electron microscopy (STEM) images (Fig. 4(b)). EDX scans collected from the same region in an attempt to determine the source of contrast do not show a deviation from the initial 2:3 atomic ratio, pointing to a mass-thickness contrast. Secondary electron SEM imaging proves this hypothesis, revealing two sets of surface structures that are referred to henceforth as the “type-I wrinkles” and “type-II wrinkles” (Fig. 4(c)). The outer diameter of type-I wrinkles matches well with the structures captured in the single-shot images. Type-II wrinkles are much larger than type-I wrinkles and show a significant difference in their periodicity. After careful examination of out-of-the-box 15 nm SiN grids and their surface structure after the multilayer coating, we concluded that the SiN membrane was not initially completely stretched over the substrate, and thus, the type-II wrinkles formed due to the impact of radiation pressure on the loose film. On the other hand, the formation of the finer scale type-I wrinkles has a more intricate mechanism.

Understanding this mechanism requires the identification of the effective parameters such as membrane thickness, coating configuration, and laser fluence. All multilayer samples discussed so far were deposited on 15 nm thick SiN membranes and irradiated with an estimated average laser peak fluence of 95.5 mJ/cm^2. To see the effect of membrane thickness, we prepared the same bilayers on 50 nm thick SiN membranes. In this case, equivalent laser irradiation results in negligible surface structuring (Fig. S2(a)). When the average laser fluence is instead increased to an average peak fluence of ~118.6 mJ/cm^2, the metal layer near the center ablates, but wrinkling is still not observed (Fig. S2(b)). Additional experiments were conducted on 15 nm SiN grids coated only with 50 nm of pure Ni with otherwise identical deposition conditions. SEM images collected from this sample after laser heating showed irregular surface structures emanating from the center (Fig. S2(c)). But even at higher laser fluences, well-ordered wrinkles were not

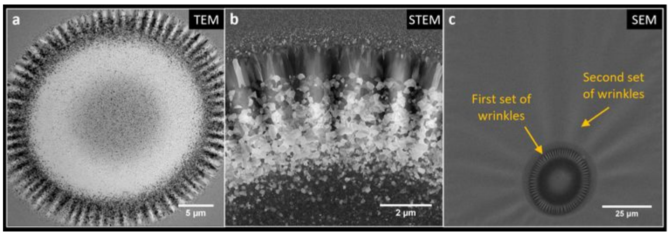

Fig. 4 Structure of the laser affected region. (a) Bright-field TEM image, (b) STEM HAADF image showing different crystal structures, (c) low magnification SEM image of the 15 nm SiN window exhibiting two types of wrinkles after laser heating.

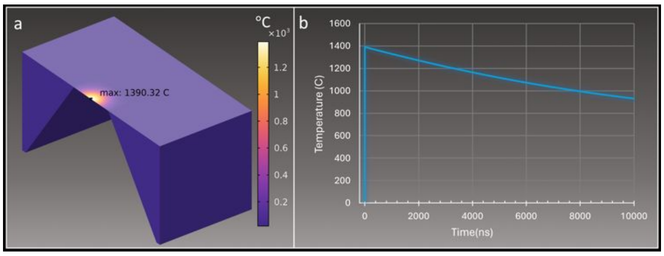

Fig. 5 Thermal finite element simulations of coating on SiN TEM grid. (a) Cross section of a single window with the temperature map showing the highest temperature of about 1390 °C at the center of the laser pulse, (b) maximum temperature profile within the first 10 μs.

obtained when the metal coating only consisted of Ni. Furthermore, Ti/Ni multilayer foils are reactive materials with exothermic reaction enthalpies contributing additional heat to the system.[41] In these multilayer structures, the reaction initiation temperature for thicker foils can be between 300°C and 400°C, providing a low energy barrier for the initiation of the exothermic reaction.[42,43] These results suggest that both the thin SiN membrane and, specifically, the Ti/Ni system plays an important role in the wrinkling process.

Thermal finite element simulations were performed using COMSOL Multiphysics software to estimate the temperature due to laser heating. The 3D geometry focuses on one window of the sample grid, including the coating, 15 nm silicon nitride membrane, and 200 μm silicon frame, as shown in Fig. 5(a). In the experimental system, the uppermost layer consists of approximately 12.6 nm of nickel. Given that the penetration depth of a 532 nm wavelength laser in nickel is about 13.3 nm, the system is approximated and modeled as a single layer of nickel with 50 nm thickness. The laser is modeled as a volumetric heat source with Gaussian spatial and temporal profiles using the average fluence and pulse width as 95.5 mJ/cm^2 and 1 ns, respectively. The index of refraction and extinction coefficient of nickel at 532 nm is 1.75 and 3.19, respectively, and can be used to obtain the reflectivity and absorption coefficient.[44] The maximum temperature from the finite element solution reaches about 1390°C within the first 5 ns and drops to about 1000°C within the first 8 μs, as shown in Fig. 5(b). This is below the melting temperature of nickel and titanium at 1455°C and 1670°C, respectively.[45] At a 2:3 atomic ratio, apart from the effect of the exothermic reaction enthalpy of the Ti/Ni system,[41] the laser energy applied to the sample is sufficient to promote the complete melting of the alloy, however unable to completely melt either pure metal system as is shown when the coating is only nickel.[45]

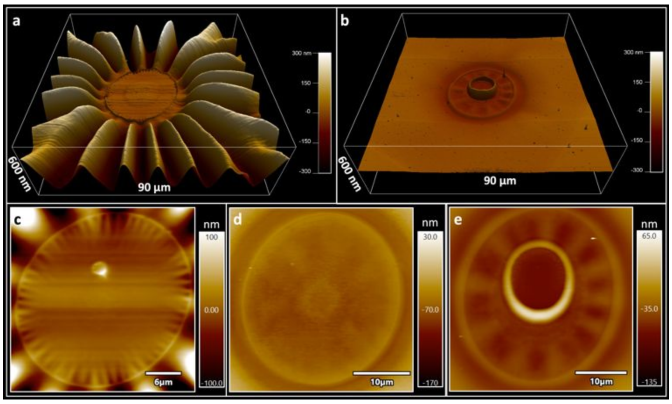

Fig. 6 AFM topography maps of samples irradiated with ~95.5 mJ/cm^2 fluence (a) on 15 nm thick SiN membrane and (b) on 50 nm thick SiN membrane. AFM height images collected from three different samples. (c) Ti/Ni coating on 15 nm membrane after laser treatment at ~95.5 mJ/cm^2 fluence, (d) on 50 nm membrane after laser treatment at ~95.5 mJ/cm^2 fluence, (e) Ti/Ni coating on 50 nm membrane after laser treatment at ~118.6 mJ/cm^2 fluence.

A complete understanding of the surface topography is studied via high-resolution AFM imaging. Fig. 6(a-b) shows 3D topography maps obtained after laser heating of Ti/Ni films on a 15 nm and 50 nm thick SiN membrane, respectively. On the thicker membrane, the film does not exhibit any surface features away from the laser-affected zone, while AFM measurements performed on the sample with the thinner membrane reveal peaks and valleys with a total 600 nm (±300 nm) height difference corresponding to type-II wrinkles. This significant difference in the neighboring region's topography for samples with different SiN film thickness is believed to result from the initial tension and thickness of the membranes. Height images of all the previously mentioned Ti/Ni coated samples, including those that irradiated with higher laser fluence, provide a full comparison (Fig. 6(c-e)). The sample on the 15 nm membrane has a flat surface at the center (except for a small surface defect just above center), and periodic wrinkles around the periphery bounded within a slightly protruding circular rim (Fig. 6(c)). The height variation along these wrinkles is measured as ± 7 nm. When similar laser fluences are used on the sample with a 50 nm membrane, the central region of this sample shows much less surface restructuring (Fig. 6(d)). The features still resemble periodic radial surface undulations, yet with a much lower frequency and amplitude compared to the thinner sample. The influence of membrane thickness on critical buckling load, which is proportional to the cube of the thickness for a rectangular cross section, is anticipated. Consequently, a thicker membrane will exhibit less buckling under the same applied load compared to a thinner membrane. Once the laser fluence is increased up to the membrane rupture threshold, the frequency and amplitude of the periodic structures increase further. The increased laser fluence also results in the formation of a new surface feature around the central region (Fig. 6(e)), and appears to have caused a combination of melting, ablation, and formation of a protruding molten ring.[23] Our experiments show that the length, height, and periodicity of the wrinkles can be tuned by changing the substrate thickness and laser fluence. Experimental SEM images of the TiNi system (Fig. 7(a)) showcase the range of the number of periods that form in the thin film after a laser pulse. A majority of the fabricated corrugated patterns are within around a range of 70-90 periods. The difference in periodicity can be attributed to the loading conditions on the multilayer thin film. Buckling and wrinkling of elastic sheets under various loading and geometric configurations have been studied extensively in the literature, theoretically and experimentally.[46–48] For ultrathin films, such experiments show deviations from the standard buckling theory and, therefore, require identifying the parameters for

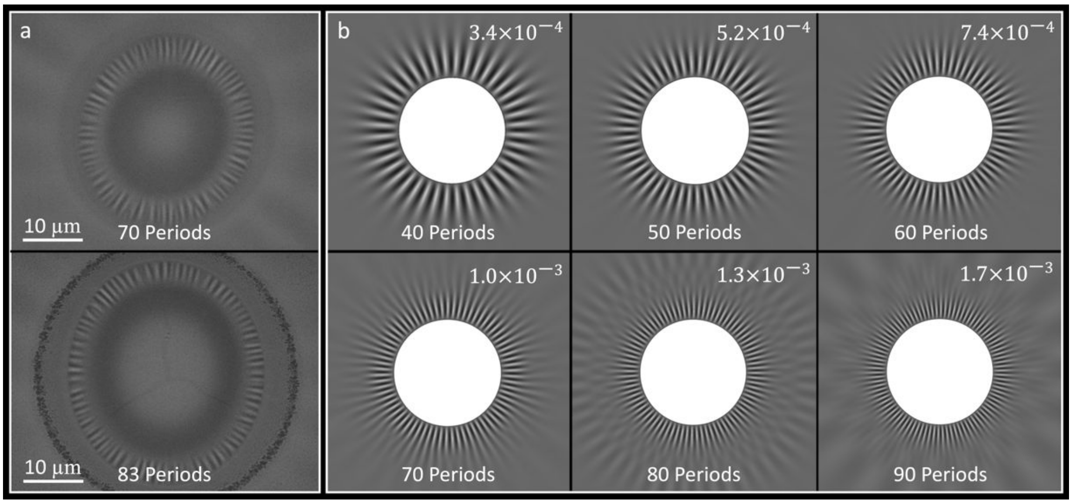

Fig. 7 Experimental and simulated wrinkle patterns. (a) Experimental images exhibiting 70 and 83 periods, (b) simulated wrinkle patterns with 40, 50, 60, 70, 80, and 90 periods corresponding to a critical buckling load show on the upper right corner of each simulated wrinkle pattern.

controlled wrinkling.[49] A model that was first studied by Lamé focuses on a very thin annular sheet under in-plane axisymmetric stress.[50] When there is a mismatch between tensile loads at the inner radius (T_{in}) and the outer radius (T_{out}), compressive hoop stress is induced in the thin film and relieved by periodic wrinkling aligned perpendicular to the compressive stress.[50] This model can be presented with a mechanical buckling analysis within the Abaqus finite element analysis software. The outer edge of the annular configuration is supported to restrict motion in all directions, and the inner edge is restricted in the out of plane direction only. In addition, a tensile load is placed on the inner edge to apply a compressive hoop stress to the model. A fine mesh created from 1000 nodes was utilized to accurately capture the large number of wrinkles. The Lanczos solver within Abaqus was used to extract the buckling modes from the analysis, which indicated an increase in the number of ordered wrinkles with an increase in the applied tensile load. Fig. 7(b) demonstrates the ordered wrinkle patterns obtained from the numerical simulations with a critical buckling load increasing from 3.4 x 10^{-4} N/mm for 40 periods to 1.7 x 10^{-3} N/mm for 90 periods. The simulations provide insight into the stress states of the thin films in the experiments, indicating a higher load for the case of the wrinkle pattern with 83 periods than the pattern with 70 periods shown in Fig. 7(a). Therefore, the periodicity can effectively be manipulated and tuned through changing processing parameters such as fluence to affect the applied load on the thin film.

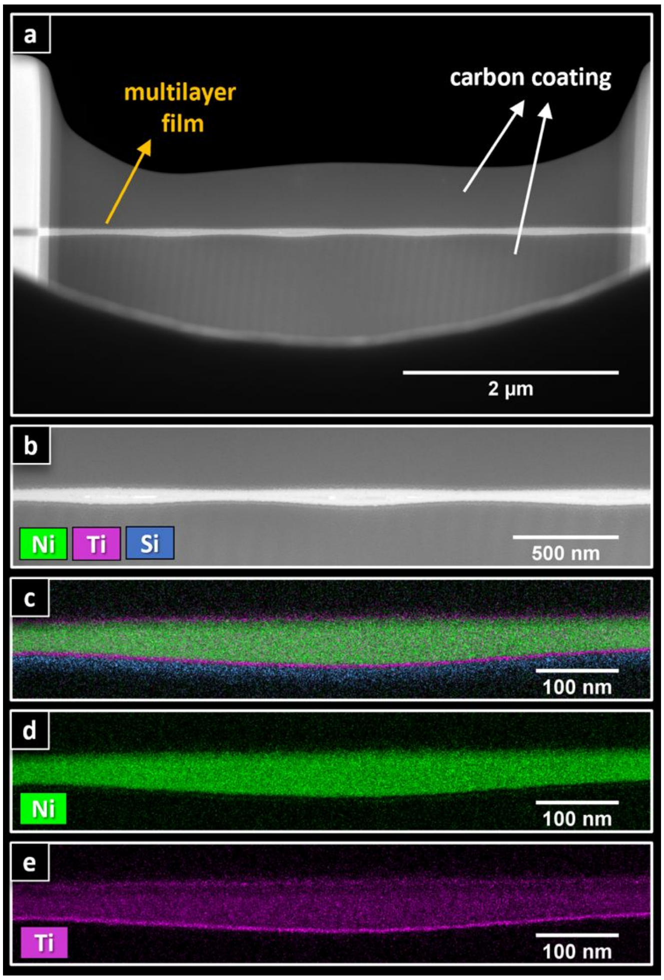

Fig. 8 Cross-sectional images and EDX maps of Ti/Ni bilayers on 15 nm SiN membrane. (a,b) STEM images collected at different magnifications showing details of the film structure. (c-e) Elemental maps of Ni, Ti, Si, and their composite image.

The results we shared so far give detailed information about the surface structure, but unlike bulk samples, laser patterning of thin films may not be limited to the top surface, such that the morphology can be controlled on both sides of the film. Therefore, characterization of the complete film profile is essential. Accordingly, we used the focused ion beam technique (FIB) to prepare a cross-sectional lift-out lamella from the specimen with 15 nm SiN membrane. The region of interest was chosen to be approximately perpendicular to several adjacent wrinkles.

Fig. 8 shows STEM-HAADF images of this lamella at different magnifications, along with EDX maps collected from one of the periodic structures. The entire film is sandwiched between two carbon layers to increase the overall sample thickness and facilitate the FIB milling process (Fig. 8(a-b)). The thin and brighter layer in the middle is the laser-irradiated Ti/Ni multilayer system on the 15 nm SiN membrane with the metal layer on top. These cross-sectional images prove the presence of periodic thickness variations at the periphery of the deformed area. Interestingly, the back side of the membrane shows significantly larger undulations than the top side, indicating deformation of the SiN membrane below the metal layer. Elemental maps of Ni, Ti, and Si display that the SiN membrane nicely follows the undulating profile of the back side without any delamination, bubble formation, or spalling (Fig. 8(c-e)). The maps also show a complete mixing of the initial Ti/Ni bilayer, supporting the proposed complete melting and then recrystallization of the metal film.

Given the single-shot UTEM data and the timescale of the dynamic process, it is apparent that wrinkle formation happens before the solidification of the molten metal layer. Therefore, it can be inferred that the wrinkle formation starts with the deformation of the SiN membrane. The wrinkling of the SiN membrane in our experiments matches the thin film Lamé model and the resulting structure well for the case of $T_{in}>T_{out}$.[50] In our samples, the development of these unmatched stresses is mainly induced thermally. The thermal gradient created by the laser between the central region and the edge could lead to tensile stress formation along the radial direction. According to the literature, thermal expansion coefficients of Ti, Ni, and SiN are 9×10^{-6} 1/°C, 12.8×10^{-6} 1/°C, and 3.3×10^{-6} 1/°C, respectively.[49,51] This difference between material properties of the substrate and the film could also contribute to the stress development and periodic wrinkle formation in the 15 nm thick SiN membrane. After wrinkle formation starts at the center of the laser spot, it propagates radially towards the periphery. A similar movement of radial wrinkles was previously observed in experiments performed on free-standing circular elastic sheets when they were impacted at their centers.[52] Considering the influence of the high-energy laser on the thin film, the out-of-plane deformations detected in the SiN membrane upon laser heating could be explained by a combined effect of thermal stresses and the radiation pressure imparted by the laser.

After such deformation of the SiN membrane, and complete melting of the metal layer, the strong radial temperature gradient at the surface would continue to affect the sample structure. This gradient in the liquid layer develops radial gradients in surface tension, and as a result, Marangoni convection flow of the molten material is triggered. Since the temperature gradient of surface tensions of Ti and Ni are negative, the redistribution of material is expected to be from the center to the periphery.[27] With the wrinkled underlying SiN membrane, the final surface structure will thus depend on the interplay between many factors, such as Marangoni forces, the solidification time of the molten layer, and gravitational forces.

Conclusions

In this study, we performed real-time imaging of periodic wrinkling and surface patterning in Ti/Ni bilayer coated thin SiN membranes via single-shot UTEM imaging. Effects of SiN membrane thickness, metal coating composition, and laser pulse energy on the final structure are discussed. Notably, both sides of the multilayer film exhibit corrugated surfaces, but with different amplitudes. Based on the experimental results, wrinkle formation starts close to the center of the laser spot and develops radially. The thin film shows a certain level of recovery in the inner parts of the heated region while the transient structures freeze at the outer boundary. After they stabilize at the boundary, lateral crystal growth propagates from the edge towards the center. As discussed previously, this particular crystal growth mechanism indicates the existence of a complete melt pool in the laser-affected area. Thermal simulations indicate an average temperature above the melting point of the 2:3 Ti:Ni atomic ratio alloy further supporting a complete melting in the affected zone. We also demonstrated that the final film structure depends on the SiN membrane thickness, laser fluence, and metal coating selection. SEM imaging and AFM height measurements present clear differences between samples prepared on SiN membranes with different thicknesses. Whereas samples on thicker (50 nm) membranes develop some radial periodic surface undulations, the amplitude and frequency are much higher for films deposited on thin (15 nm) membranes. At higher laser pulse energies, wrinkles become even easier to detect with increased amplitude and frequency, while ablation and, hence, hole formation are also detected near the center of the laser illumination spot. This is further corroborated through mechanical thin film wrinkling simulations with larger applied loads leading to an increase in the frequency of the ordered structures. The highly ordered periodic structures do not form when the metal coating is only Ni, thereby confirming the significance of the composition of the metal layer. Lastly, STEM imaging of sample cross-sections reveals undulations on both sides of the film with different amplitudes, indicating deformation of the SiN membrane. The physics of wrinkling and buckling remains a complicated phenomenon but has a crucial role in applications like diffraction gratings, lithography masks, pressure sensors, and functional coatings. The findings of this work, the first comprehensive experimental in-situ study on laser-induced periodic wrinkling of ultrathin multilayer films, could enable future laser-irradiation-based fast fabrication of corrugated films for tailored properties and applications.

Author Contributions

V.O. conceived the project and designed the experiments. V.O. performed the UTEM experiments and T.I. took the experimental notes. T.I. performed the conventional TEM and SEM/FIB imaging. M.F. carried out electron diffraction analysis, thermal and mechanical numerical simulations, and helped with the sample preparation. W.L. and B.D.H. performed and analyze the AFM measurements. All authors discussed the results and commented on the manuscript.

Conflicts of interest

There are no conflicts to declare.

Acknowledgements

This work was supported by the Young Investigator Program of Department of Defense Office of Naval Research (Grant number FA9550-21-1-0396) and the Multidisciplinary University

Research Initiative Program of Department of Defense Office of Naval Research (Grant number FA9550-19-1-0008). B.D.H. and W.L. appreciate support from the UConn Institute of Materials Science. The authors would like to acknowledge the help of Ali Gokirmak and Saidjafarzoda Ilhom for electron beam evaporation.

Notes and references

‡ Footnotes relating to the main text should appear here. These might include comments relevant not central to the matter under discussion, limited experimental and spectral data, and crystallographic data.
§
§§
etc.

1 E. P. Chan, E. J. Smith, R. C. Hayward and A. J. Crosby, *Adv. Mater.*, 2008, **20**, 711–716.

2 P.-C. Lin and S. Yang, *Soft Matter*, 2009, **5**, 1011–1018.

3 J. Y. Chung, J. P. Youngblood and C. M. Stafford, *Soft Matter*, 2007, **3**, 1163–1169.

4 Y. Ebata and A. J. Crosby, *Soft Matter*, 2014, **10**, 1963–1968.

5 J. Y. Chung, A. J. Nolte and C. M. Stafford, *Adv. Mater.*, 2011, **23**, 349–368.

6 T. Xie, X. Xiao, J. Li and R. Wang, *Adv. Mater.*, 2010, **22**, 4390–4394.

7 J. Yin, J. L. Yagüe, D. Eggenspieler, K. K. Gleason and M. C. Boyce, *Adv. Mater.*, 2012, **24**, 5441–5446.

8 E. Cerda, K. Ravi-Chandar and L. Mahadevan, *Nature*, 2002, **419**, 579–580.

9 G. Reiter, M. Hamieh, P. Damman, S. Sclavons, S. Gabriele, T. Vilmin and E. Raphaël, *Nat. Mater.*, 2005, **4**, 754–758.

10 J. Huang, M. Juszkiewicz, W. H. de Jeu, E. Cerda, T. Emrick, N. Menon and T. P. Russell, *Science*, 2007, **317**, 650–653.

11 J. Y. Chung, A. J. Nolte and C. M. Stafford, *Adv. Mater.*, 2009, **21**, 1358–1362.

12 C. M. Stafford, C. Harrison, K. L. Beers, A. Karim, E. J. Amis, M. R. VanLandingham, H.-C. Kim, W. Volksen, R. D. Miller and E. E. Simonyi, *Nat. Mater.*, 2004, **3**, 545–550.

13 N. Bowden, S. Brittain, A. G. Evans, J. W. Hutchinson and G. M. Whitesides, *Nature*, 1998, **393**, 146–149.

14 J. Groenewold, *Phys. Stat. Mech. Its Appl.*, 2001, **298**, 32–45.

15 E. Cerda and L. Mahadevan, *Phys. Rev. Lett.*, 2003, **90**, 074302.

16 N. Uchida, *Phys. Nonlinear Phenom.*, 2005, **205**, 267–274.

17 J. Genzer and J. Groenewold, *Soft Matter*, 2006, **2**, 310–323.

18 J. Narayan, *JOM*, 1980, **32**, 15–21.

19 V. P. Veiko and V. I. Konov, Eds., *Fundamentals of Laser-Assisted Micro- and Nanotechnologies*, Springer International Publishing, Cham, 2014, vol. 195.

20 M. Olbrich, E. Punzel, P. Lickschat, S. Weißmantel and A. Horn, *Phys. Procedia*, 2016, **83**, 93–103.

21 B. Voisiat, M. Gedvilas, S. Indrišiūnas and G. Račiukaitis, *Phys. Procedia*, 2011, **12**, 116–124.

22 T. T. D. Huynh, A. Petit and N. Semmar, *Appl. Surf. Sci.*, 2014, **302**, 109–113.

23 F. Korte, J. Serbin, J. Koch, A. Egbert, C. Fallnich, A. Ostendorf and B. N. Chichkov, *Appl. Phys. A*, 2003, **77**, 229–235.

24 U. J. Lorenz and A. H. Zewail, *Science*, 2014, **344**, 1496–1500.

25 X. Fu, B. Chen, J. Tang, M. Th. Hassan and A. H. Zewail, *Science*, 2017, **355**, 494–498.

26 S. T. Park, D. J. Flannigan and A. H. Zewail, *J. Am. Chem. Soc.*, 2011, **133**, 1730–1733.

27 O. Bostanjoglo and T. Nink, *Appl. Surf. Sci.*, 1997, **109–110**, 101–105.

28 V. Yu. Balandin, D. Otte and O. Bostanjoglo, *J. Appl. Phys.*, 1995, **78**, 2037–2044.

29 T. Nink, F. Galbert, Z. L. Mao and O. Bostanjoglo, *Appl. Surf. Sci.*, 1999, **138–139**, 439–443.

30 T. LaGrange, M. R. Armstrong, K. Boyden, C. G. Brown, G. H. Campbell, J. D. Colvin, W. J. DeHope, A. M. Frank, D. J. Gibson, F. V. Hartemann, J. S. Kim, W. E. King, B. J. Pyke, B. W. Reed, M. D. Shirk, R. M. Shuttlesworth, B. C. Stuart, B. R. Torralva and N. D. Browning, *Appl. Phys. Lett.*, 2006, **89**, 044105.

31 T. LaGrange, G. H. Campbell, B. W. Reed, M. Taheri, J. B. Pesavento, J. S. Kim and N. D. Browning, *Ultramicroscopy*, 2008, **108**, 1441–1449.

32 O.-H. Kwon, B. Barwick, H. S. Park, J. S. Baskin and A. H. Zewail, *Proc. Natl. Acad. Sci.*, 2008, **105**, 8519–8524.

33 H. S. Park, O.-H. Kwon, J. S. Baskin, B. Barwick and A. H. Zewail, *Nano Lett.*, 2009, **9**, 3954–3962.

34 J. T. McKeown, N. A. Roberts, J. D. Fowlkes, Y. Wu, T. LaGrange, B. W. Reed, G. H. Campbell and P. D. Rack, *Langmuir ACS J. Surf. Colloids*, 2012, **28**, 17168–17175.

35 B.-K. Yoo, O.-H. Kwon, H. Liu, J. Tang and A. H. Zewail, *Nat. Commun.*, 2015, **6**, 8639.

36 B. Chen, X. Fu, J. Tang, M. Lysevych, H. H. Tan, C. Jagadish and A. H. Zewail, *Proc. Natl. Acad. Sci.*, 2017, **114**, 12876–12881.

37 P. K. Olshin, J. M. Voss, M. Drabbels and U. J. Lorenz, *Struct. Dyn.*, 2020, **7**, 011101.

38 Y. Zhang, Z. Li, Z. Li, J. Li, J. Li and H. Yang, *J. Phys. Chem. C*, 2022, **126**, 20929–20936.

39 G. C. Egan, T. LaGrange and M. R. Zachariah, *J. Phys. Chem. C*, 2015, **119**, 2792–2797.

40 A. J. Birnbaum, Y. L. Yao, U.-J. Chung, James. S. Im, X. Huang and A. G. Ramirez, *Appl. Phys. Lett.*, 2009, **94**, 261908.

41 F. R. de Boer, W. C. M. Mattens, R. Boom, A. R. Miedema and A. K. Niessen, *Cohesion in metals. Transition metal alloys*, North-Holland, Netherlands, 1988, vol. 1.

42 D. P. Adams, M. A. Rodriguez, J. P. McDonald, M. M. Bai, E. Jones Jr., L. Brewer and J. J. Moore, *J. Appl. Phys.*, 2009, **106**, 093505.

43 A. J. Cavaleiro, A. S. Ramos, R. M. S. Martins, F. M. B. Fernandes, J. Morgiel, C. Baehtz and M. T. Vieira, *J. Alloys Compd.*, 2015, **646**, 1165–1171.

44 E. D. Palik, Ed., in *Handbook of Optical Constants of Solids*, Academic Press, Burlington, 1997, pp. xv–xviii.

45 K. Otsuka and X. Ren, *Mater. Sci. Eng. A*, 1999, **273–275**, 89–105.

46 H. Tian, L. Chen and B. Li, *Int. J. Numer. Methods Eng.*, 2023, **124**, 2014–2033.

47 M. Taylor, B. Davidovitch, Z. Qiu and K. Bertoldi, *J. Mech. Phys. Solids*, 2015, **79**, 92–107.

48 W. Huang, W. Yan, R. Xu, Q. Huang, J. Yang, F. Trochu and H. Hu, *Thin-Walled Struct.*, 2021, **161**, 107512.

49 J. Carvill, in *Mechanical Engineer's Data Handbook*, ed. J. Carvill, Butterworth-Heinemann, Oxford, 1993, pp. 218–266.

50 B. Davidovitch, R. D. Schroll, D. Vella, M. Adda-Bedia and E. A. Cerda, *Proc. Natl. Acad. Sci.*, 2011, **108**, 18227–18232.

51 C.-L. Tien and T.-W. Lin, *Appl. Opt.*, 2012, **51**, 7229–7235.

52 R. Vermorel, N. Vandenberghe and E. Villermaux, *Proc. R. Soc. Math. Phys. Eng. Sci.*, 2008, **465**, 823–842.

Data availability statement

The data supporting the findings of this study are included within the article and its ESI files. Further data that support the findings of this study are available from the corresponding author upon reasonable request.